SURFACE GRAVITY WAVE STATISTICS FROM STEREO VIDEO

by

Zachary J. VanKirk

A thesis submitted to the Faculty of the University of Delaware in partial fulfillment of the requirements for the degree of Master of Science in Marine Studies

Spring 2013

SURFACE GRAVITY WAVE STATISTICS FROM STEREO VIDEO

by

Zachary J. VanKirk

Approved: _____

Fabrice Veron, Ph.D.
Professor in charge of thesis on behalf of the Advisory Committee

Approved: _____

Mark A. Moline, Ph.D.
Director of the School of Marine Science and Policy

Approved: _____

Nancy M. Targett, Ph.D.
Dean of the College of Earth, Ocean, and Environment

Approved: _____

James G. Richards, Ph.D.
Vice Provost for Graduate and Professional Education

TABLE OF CONTENTS

LIST OF FIGURES

ABSTRACT

A stereo imaging system was deployed during a 2010 field experiment aboard R/P FLIP to study small scale surface gravity waves under a wide range of conditions. A novel variational and cross correlation based algorithm is presented which generates 3-dimensional depth maps of the ocean surface from stereo digital video images. This thesis details the hardware and software used in this investigation and characterizes the wave field in space and time. Waves ranging from approximately $5cm < \lambda < 2m$ are resolved propagating through the $4m \times 4m$ camera footprint. Good agreement is shown with optical wave-gauge data. Spectral statistics show good agreement with other investigations at similar scales. The surface height frequency spectrum is of the form f^{-4}, while the omnidirectional wavenumber spectrum is shown to be of the form k^{-3}. Peak-wave phase-averaged variances are then presented for distinct wavenumber bands, showing a propensity for small waves to group at long-wave crests.

Chapter 1

INTRODUCTION

Much attention has been given recently to secular changes in the world climate, the so-called "global warming." Much of the discussion has been related to the atmospheric increase in greenhouse gasses such as carbon dioxide (CO_2). Although many of the details are not yet well understood, it is known that the global oceans are a large sink for heat, moisture, and trace gasses such as (CO_2). It has also been shown that feedback loops may be important; the increasing temperatures may decreases the ocean's capacity to store (CO_2), reinforcing the warming trend (*Le Quéré et al.*, 2007).

At the air-sea interface, wave related phenomena such as wave breaking, bubble entrainment, the generation of sea spray, and wind-wave interaction significantly influence the transfers of heat, mass, and moisture between the the ocean and atmosphere. These transfers in turn impact meteorological conditions over many time scales. Therefore, a deeper knowledge of the physics occurring at the air-sea interface is necessary if we are to better understand and forecast global climate trends.

To illustrate the importance of surface gravity waves, one can think of the life-cycle of such a wave. As wind increases, waves grow. This increases ocean roughness and creates drag. Surface waves can significantly modify the wind velocity profiles above them (*Banner and Melville*, 1976). The waves continue to grow, and eventually begin to occasionally break. When a wave becomes too steep, seawater slides and/or plunges down the wave face, entraining air bubbles below the surface and creating turbulence and inducing mixing. It has been estimated that including wave breaking effects may increase previous estimates of (CO_2) air-sea transfer velocity by a factor

of 2-4 (*Melville*, 1996).

Small scale surface gravity waves are of particular interest for remote sensing applications. Radar backscatter is used to estimate sea surface height and roughness from land, ships, aircraft, and satellites. Many of these instruments, including COastal raDAR (CODAR) and Synthetic Aperture Radar (SAR), are sensitive to ocean waves with short and intermediate wavelengths ($\lambda < 50m$). The sea-surface height and roughness estimates from the backscatter data are also used as proxies for other valuable quantities such as current velocities, wind speed, and gas transfer velocities (*Liu*, 2002; *Naderi et al.*, 1991). In order to maximize the accuracy of these estimates, the spatial and temporal distributions of short gravity waves must be directly measured; the relationships between waves and other processes occurring at the interface must be well understood.

Earlier measurements of short waves were largely constrained to wave frequency spectra obtained from capacitance wire probes (*Banner*, 1989). The problem with this approach is that it is difficult to retrieve spatial information from point measurements due to the doppler shifting of short waves by long waves. As small waves propagate, they are advected by periodic surface currents generated by the underlying swell. It is therefore necessary to measure the waves' spatial distribution directly. In order to recover spatial representations of short gravity waves, multiple locations must be sampled near instantaneously. This can be accomplished using an array of wave gauges, or conveniently by capturing and analyzing digital images of the wave field.

Stereo imaging has been utilized to study ocean waves by *Banner* (1989), *Gallego et al.* (2008), *Shemdin et al.* (1988) and *Wanek and Wu* (2006). This method is accomplished by taking simultaneous digital images of a scene, determining the location of corresponding features in those images, and using the geometry of the camera system in order to recover a 3-D representation of the scene relative to the cameras.

Many computational approaches have been used to identify corresponding features; a review and evaluation of current matching algorithms is given in *Scharstein and Szeliski* (2002).

An accurate 3-Dimensional representation of the wave field can be difficult to attain Using this approach. For instance, features visible in one camera perspective may not be visible in another perspective due to specular reflection and occlusion. In addition, the direct reflection of rays of sunlight into the digital camera, referred to as sun glitter, results in saturation of the images. A theoretical review of the inherent limitations of imaging ocean waves is provided in *Jähne and Waas* (1994). There is also the practical problem of keeping small waves in focus as the target moves toward and away from the camera with the long waves. These concerns can be substantially mitigated in several ways. First, using high resolution cameras allows for a large number of data points, which then can be filtered to remove poor matches caused by reflection and occlusion. Images should be taken when the sun is low in the sky or obstructed by clouds to minimize sun glitter. Maintaining a large range of focus can either be achieved by adjusting the lens focus dynamically or by having the lens sufficiently far from the target and focused at optical infinity.

An experiment was undertaken on R/P FLIP from June 5 to June 19 2010 off the coast of Santa Rosa, CA (38.34° N 123.43° W) (figure 1.1) as part of the High Resolution Air-Sea Interaction experiment (HIRES 2010). The ocean depth was 165 m. R/P FLIP, or FLoating Instrument Platform, is a 102 m research vessel which is designed to fill ballasts in order to pitch 90° (flip), such that 91 m of the platform remains below the ocean surface (see figure 1.2 for an image of R/P FLIP in its "upright" position). Most of FLIP's mass is far below the influence of the surface waves, making the platform relatively stable. Starboard, port, and front boom extend $\approx 20\,m$ from the vessels' upright hull. These characteristics make R/P FLIP ideal for air-sea interaction studies. The main goal of the experiment was to investigate statistical and

dynamical properties of surface gravity waves. To better understand wave interactions and evolution, surface wave height measurements were collected at many scales, ranging in wavelength from centimeters to kilometers. Several instrument packages were deployed by other investigators including optical wave gauges, scanning LIDAR, stereo infrared cameras, wind profilers, wave-ADCPs, and IMU/GPS units. This work focuses on a visible wavelength stereo imaging system which was developed to investigate a specific wavenumber range ($1cm < \lambda < 2m$).

Conditions during the experiment varied widely, with 10-m wind speed U_{10} and significant wave height H_s varying from 1 to 20 m/s and 1 to 5 m, respectively. Figure 1.3 details the wind and wave conditions throughout the experiment. It is of note that extreme winds and currents were forced the experiment to be cut short by several weeks. A deep current caused R/P FLIP to list 10° to starboard, eventually causing one of three mooring lines to break.

The organization of this document thesis is as follows: Chapter 2 will explore in detail the hardware used in this investigation and the software developed to analyze the raw images taken from the stereo system. Chapter 3 will present frequency, directional, and omnidirectional wavenumber spectra for selected periods during the experiment. These data will then be compared to other investigations in the literature. In addition, peak-wave phase averaged spectra are provided to investigate the influence of large surface waves on the smaller waves measured by the stereo system.

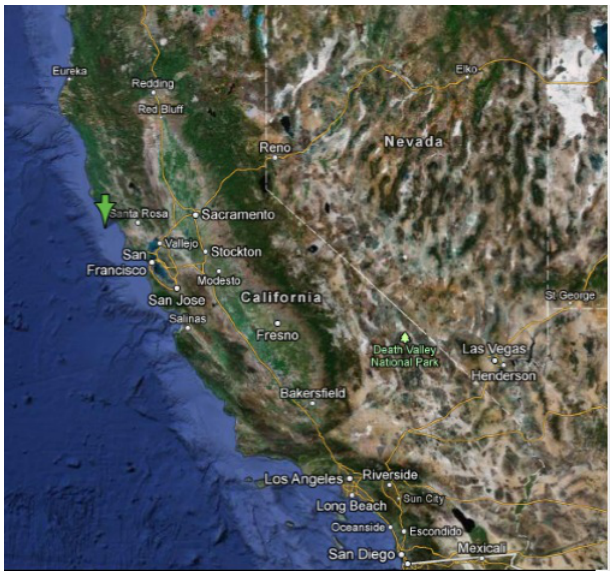

Figure 1.1: Location of R/P FLIP during HIRES 2010. Imagery 2013 TerraMetrics, Map data 2013 Google

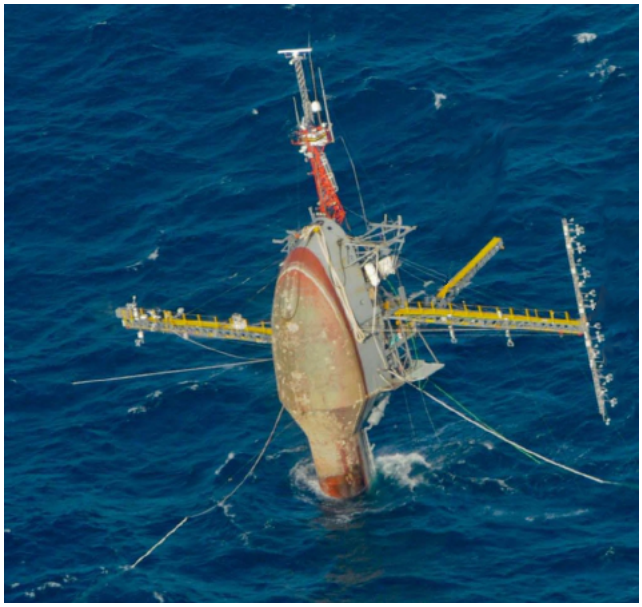

Figure 1.2: View of R/P FLIP from the air in June 2010 off the coast of northern California

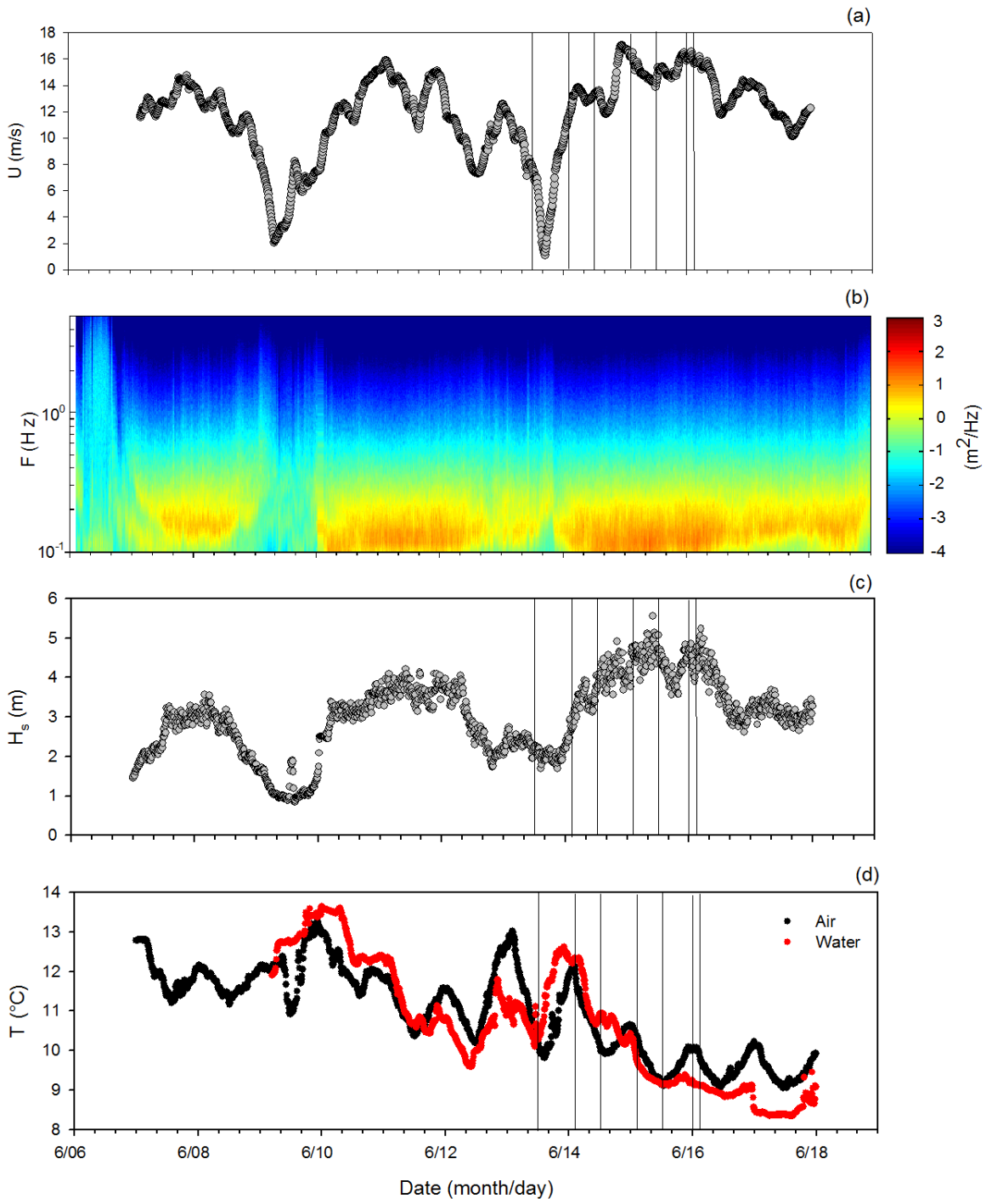

Figure 1.3: Conditions during the HIRES 2010 experiment: (a) mean U10, (b) frequency spectrogram of the surface elevation, (c) significant wave height (d) air and water surface temperatures. Vertical lines indicate when datasets used in this thesis were taken.

Chapter 2

TECHNIQUES: GENERATING 3-D DEPTH MAPS FROM STEREO IMAGES

This chapter will detail the hardware and software used for the stereo visible imaging system deployed during HIRES 2010.

2.1 Hardware

Two 4-megapixel (Jai-Pulnix RM-4200) cameras were deployed on the starboard boom of R/P FLIP, roughly $10m$ above the mean water level. The baseline between the two cameras was 3.26 m. The cameras were oriented with a 24 degree tilt from the vertical, and a convergence angle of 19.75 degrees. Simultaneous images of the ocean surface from the left and right cameras were acquired at $10Hz$ for ten minutes at the top of every hour. A Riegl LD-90 optical wave gauge was deployed at the end of the starboard boom for comparison, and a Hemisphere differential GPS receiver and two inertial motion units deployed on the starboard boom provided location and acceleration information throughout the experiment. Figure 2.1 details the location of the instruments aboard R/P FLIP.

The cameras were housed in PELCO EH2515 enclosures. They each contained a 12v power supply, camera-link to fiber optic transducer (RCX C-link), camera, Birger Engineering EF lens controller, and a Cannon $35mm$ 1.4L lens. Figure 2.2 illustrates the contents housed in the enclosure. In this configuration, the average camera footprint was roughly $4m \times 4m$. The aperture and focus of the lens was controlled remotely via serial connection to the Birger lens controller. This allowed for remote adjustment of the camera as the ambient light intensity and sea-state changed throughout the day.

The aperture and shutter speed were adjusted 5 minutes before each acquisition run to maximize depth of field and image sharpness.

Converting the camera-link signal to an optical signal provided several benefits. RCX C-link units manufactured by EDT were used for this purpose. They not only made deployment easier, but extended the distance between camera and computer past the camera-link length maximum of 10 meters. Two transducers were needed for each camera, one plugged into the framegrabber and one into the camera. The $10Hz$ digital trigger and the serial signal to control the lens were also transmitted through the fiber optic cable. A Matrox Solios eCL dual-base camera-link frame grabber, together with IO Industries Streams5 software, was used to recover the video data, which was then stored on a RAID array.

2.2 Matching Algorithm

A matching algorithm was developed to convert the 12-bit monochrome images of the ocean surface to depth maps $z = f(X, Y)$, where X and Y are world coordinates relative to a stationary geographic location. This was accomplished by identifying matching areas in the left and right image frames and using the camera geometry to recover the distance from the camera to the object. Matching areas are determined by dividing the left image into uniform square sections, then algorithmically searching for matching areas in the right image. This process is comprised of ten steps; a flow chart is provided for reference in Figure 2.3.

Before the images are processed, a mooring line which intermittently passed through the field of view during the experiment must be removed[1]. This is accomplished by performing a Radon transform, which estimates the location and orientation

[1] A wind direction which varied from wind model estimations prior to the experiment caused R/P FLIP to rotate away from its intended orientation and bring a mooring line into the field of view.

of linear objects in the images. The Radon transform is the projection of the image intensity along a radial line oriented at a specific angle (see Figure 2.4).

Next, the mean image is subtracted from each individual frame. This is done to eliminate static aspects of the images caused by the optics, CCD, and any artifacts on the lens or housing windows. To accomplish this, the average intensity value at each pixel is calculated over an ensemble of 6000 images corresponding to each 10-minute data set. The data set mean is then subtracted from each image.

Corresponding images from the left and right cameras are then rectified using an algorithm developed by *Fusiello and Irsara* (2008). The rectification process uses the geometry of the stereo camera system to warp the images in such a way that the search for corresponding areas in the image pairs is constrained to the same horizontal row on both rectified images. This greatly reduces the algorithm's computation time. The rectification algorithm uses a list of matched points provided by the investigator to recover the camera geometry. This is often referred to in the literature as uncalibrated stereo rectification. Figure 2.5 shows an example of two corresponding images before and after rectification.

The pre-processed images are then analyzed using a pyramid-type, variational, cross-correlation based matching routine. This approach is a combination of several methods used by other investigators. Pyramid type area based cross-correlation matching algorithms have been used frequently for at least twenty years, an overview of this technique is provided in *Cochran and Medioni* (1992). Variational methods, which minimize a global energy function, are also popular and an active area of research (*Faugeras and Keriven*, 2002). It was found that the variational approach is superior in resolving the large scale features in the images and is less prone to false matches while the cross-correlation method is superior at fine scales. Therefore, a hybrid algorithm was used in which the techniques are performed in series. It is useful here to

introduce the concept of a disparity map. The disparity is defined as the horizontal distance, in pixels, between matching areas in the left and right rectified image frames. The disparity map is given as $D = f(x, y)$, where each D is the distance in pixels between an abject or feature in the left and right images. For example, in Figure 2.5b, a group of small waves is identified at $x = 800\,px$ and the same group can be seen in the right image at $x = 600\,px$. For this case, the disparity $D = -200\,px$ and is a measure of the distance between the camera and this feature on the surface. As such, an accurate disparity map is the goal of all stereo matching algorithms. For this implementation, a hybrid cross-correlation and variational based matching algorithm is used which utilizes cascading window sizes to gain spatial resolution. The final window size is 8×8 pixels with a 50 % overlap .

The variational portion of the matching algorithm is comprised of 3 pyramid levels, corresponding to matching areas of 2^n pixels squared where $n = 8, 7, 6$. At each level, the algorithm iteratively minimizes a cost functional, the weighted sum of a cross correlation term and a surface curvature term:

$$E(D) = \alpha E(D)_{xcorr} + \beta E(D)_{curv} \tag{2.1}$$

The gradient of the maximum correlation value at each location is $E(D)_{xcorr}$ and the regularization term, $E(D)_{curv}$, is the surface curvature at each location. Tuned weighting parameters α and β are a function of the pyramid level. By minimizing a functional which is the weighted sum of these two terms, we arrive at a final disparity map at each level which has both a high cross-correlation between matched areas and is relatively continuous. The gradient of the cross-correlation, $E(D)_{xcorr}$, is estimated using the difference of two cross correlations on either side of the disparity estimate, as shown in Figure 2.6. The regularization term, $E(D)_{curv}$, is needed to reduce false matches which imply a discontinuous ocean surface.

At the first pyramid level of the variational matching routine, the disparity map D is initialized with a mean disparity guess based on the measured distance to the ocean surface derived from a nearby optical wave gauge. To verify that the data were not biased by using this estimate, an independent version of the algorithm was developed which instead uses the global cross-correlation between the left and right images. This algorithm takes longer to converge on a nearly identical disparity map.

After the disparity map has converged to minimize $E(D)$, it is interpolated to a higher resolution grid and used as a first guess for the next pyramid level. The process is then repeated at the new level. This proceeds until the final variational disparity map is reached, with a matching area of 64×64 pixels. This result is used to initialize the cross-correlation portion of the matching algorithm, which includes subpixel interpolation. The normalized cross-correlation value for each point in the new disparity map is saved for later use. An example of a final disparity map, with a matching area of 16x16 pixels, is given in Figure 2.7. The y-axis gradient in disparity is a result of the cameras being tilted 24° from vertically downward; this causes objects near the top of the camera's FOV to be farther away than those near the bottom.

Using the calibration information detailed previously, and the measured distance between the two camera CCDs, each point in the disparity map is triangulated to a point in 3-D space relative to the left camera. This is accomplished using the Camera Calibration toolbox developed by *Bouguet* (2011).

The result is a point cloud with each (X, Y, Z) triplet corresponding to a matched area in the left image, where the capital letters denote triangulated coordinates in meters. The location of the points is then rotated using the pitch, roll, and yaw measurements from an inertial motion unit deployed $2.25m$ forward from the camera baseline on the starboard boom. The average mean plane is then calculated using all point-clouds in the ten minute dataset. Since the mean ocean surface for the ten minutes

measure is very nearly flat, the point clouds are then rotated such that the new mean plane is also flat. This rotation accounts for the angle of the cameras relative to the flat mean ocean surface. An example of a rotated 3-D point cloud is provided in Figure 2.8.

Finally the point cloud is interpolated to a regular grid $Z = f(X, Y)$, where capital letters denote world coordinates. Figure 2.9 shows the 3-D depth map after the interpolation of the (X, Y, Z) triplets from figure 2.8. After this step has been completed for all image pairs, the result is a (X, Y, Z, t) data cube of surface elevations.

In order to validate the stereo software, the mean height from the stereo system over the entire footprint was compared with the mean water level height detected by a single point laser wave gauge. Figure 2.10 shows time series of the mean water levels from both instruments and shows that agreement is quite good ($r^2 = 0.96$).

In this configuration, a 8×8 pixel window corresponds to a spatial resolution of approximately $1.2 \times 1.2\,cm$ at a range of 8 meters or $1.6 \times 1.6\,cm$ at a 10 meter range. Also, a disparity difference of one pixel corresponds to a range difference of approximately $6.2\,mm$ With this in mind, it is conservatively estimated that features with length scales of between .05 and 2 meters should be detected with a range accuracy of at least 1 cm.

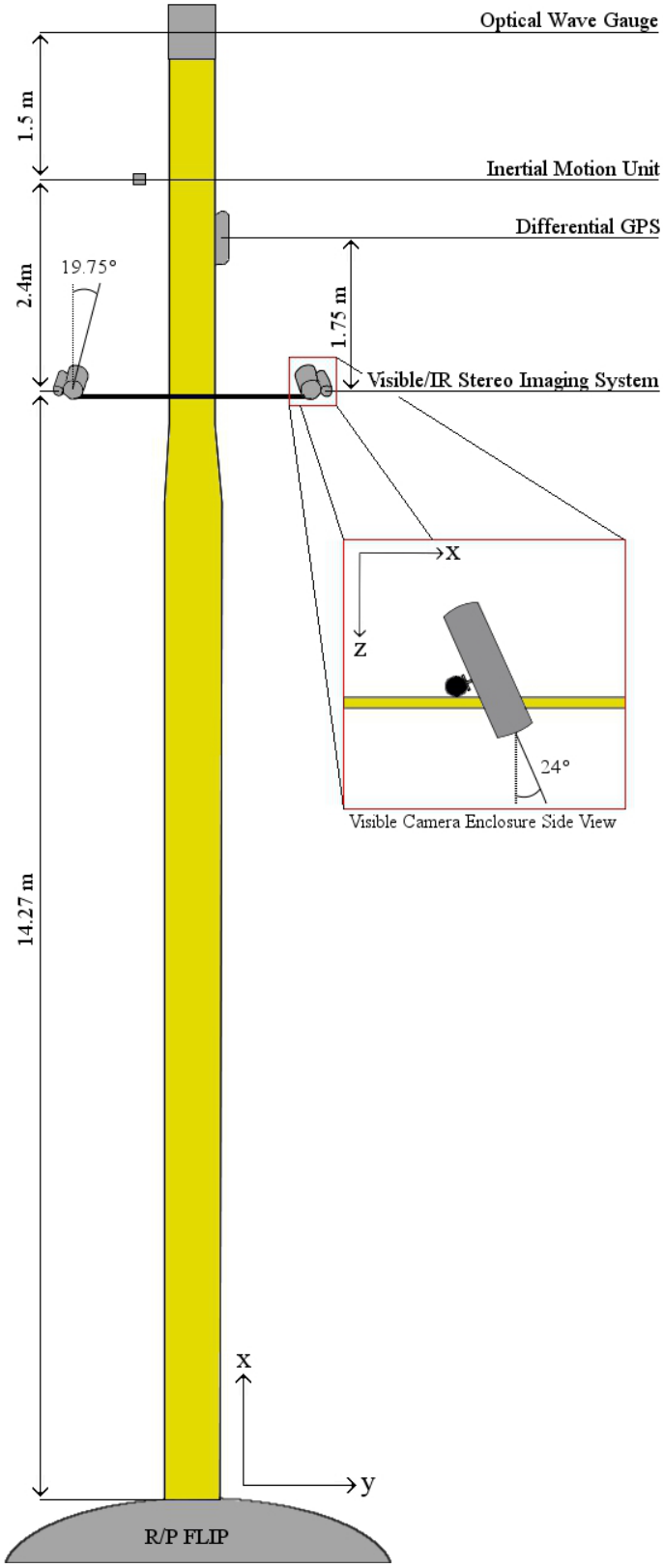

Figure 2.1: Schematic of selected instruments deployed on starboard boom of R/P FLIP in June 2010

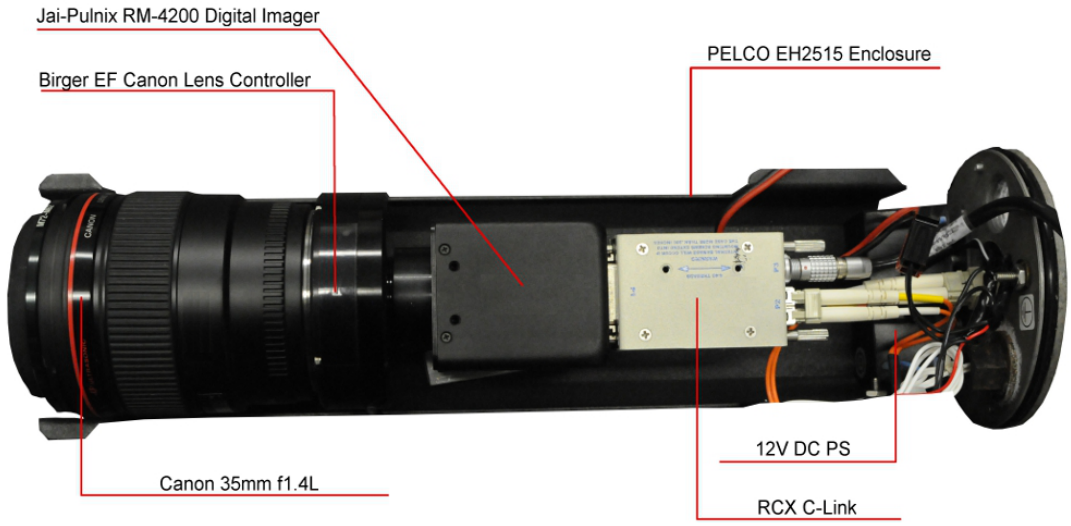

Figure 2.2: Diagram of the hardware used in the camera enclosure

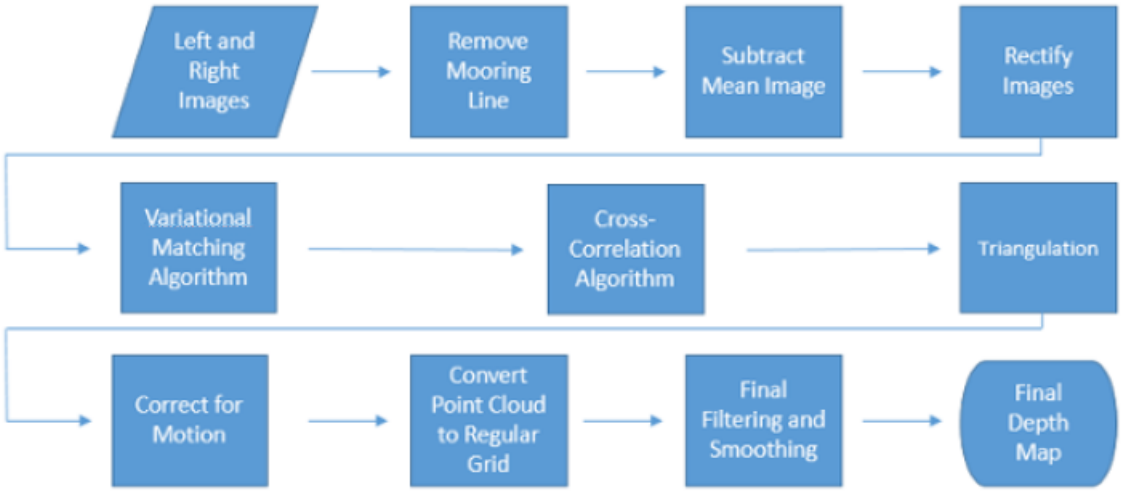

Figure 2.3: Flow chart illustrating each step a pair of images must undergo before a 3-D depth map is generated

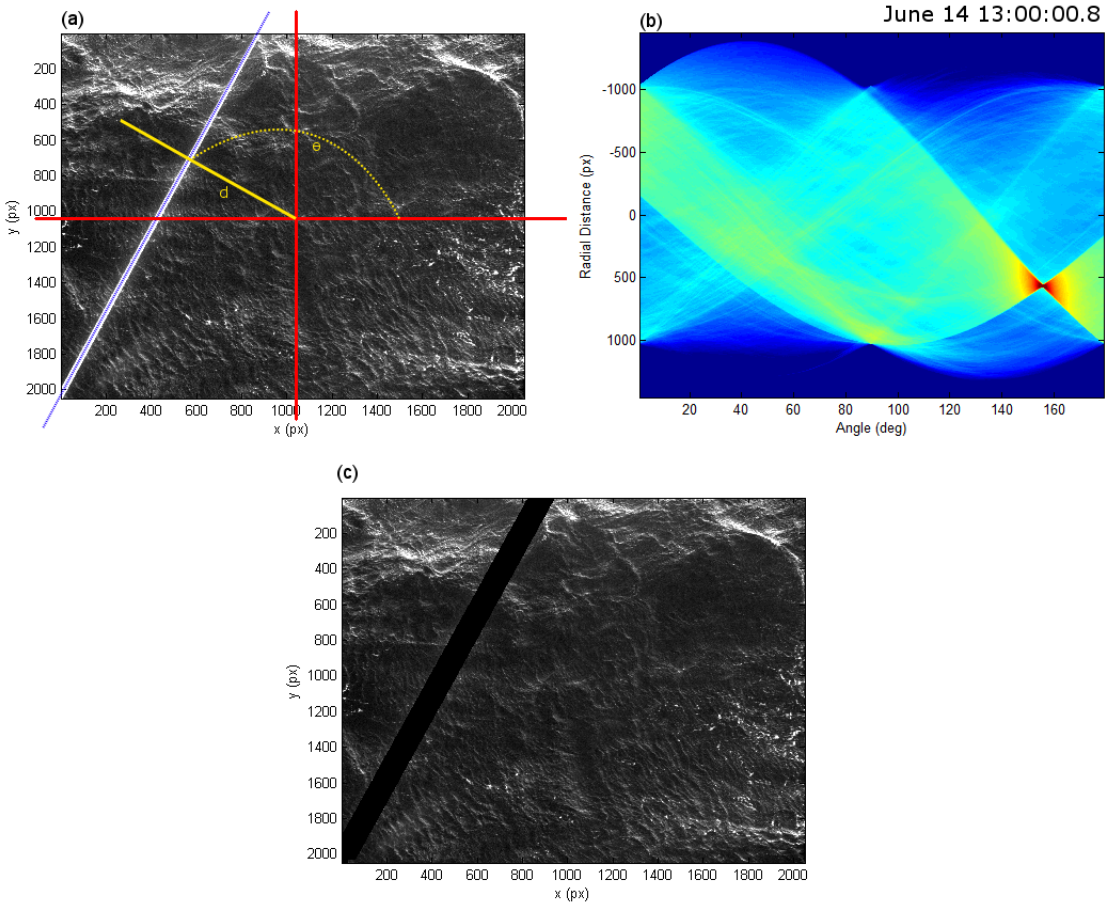

Figure 2.4: (a): monochrome image of ocean waves with mooring line highlighted. The Radon transform sums the intensities along perpendicular lines for each (d, θ) coordinate (b) visualization of the Radon transform of the image. The peak at $\theta \approx 150°, d \approx 500\,px$, represents the mooring line. (c) using the result from the Radon transform, the mooring line is dynamically removed in each images.

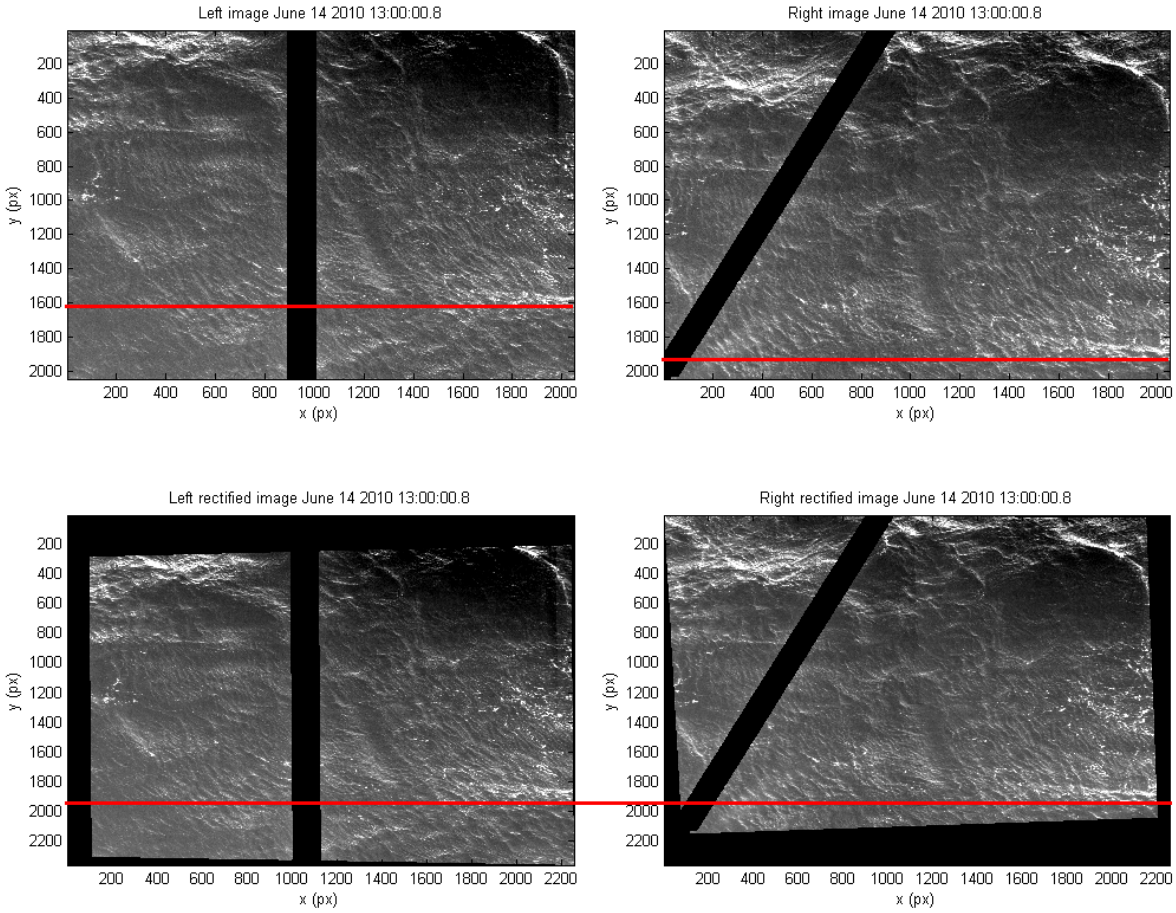

Figure 2.5: Illustration of the stereo rectification process. Top row: instantaneous raw images from the left and right cameras. Bottom row: rectified images with the mooring line removed. Notice, for reference the linear feature at bottom right in both images now lies at the same ys coordinate in both rectified images.

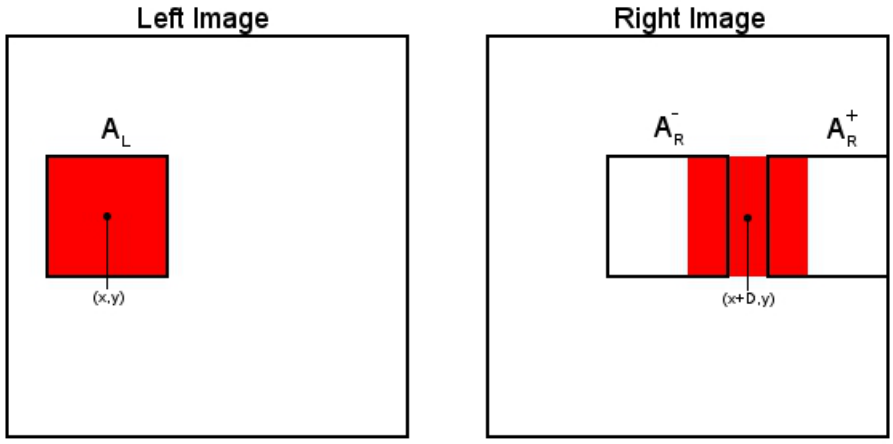

Figure 2.6: Approximately matched windows are represented by the shaded areas above. The difference between the x coordinate in the left and right images is the disparity, $D = f(x, y)$. The correlation gradient is estimated at each point in the disparity map by calculating the difference of the maximum cross correlation between areas A_L and A_R^+, and A_L and A_R^-, respectively.

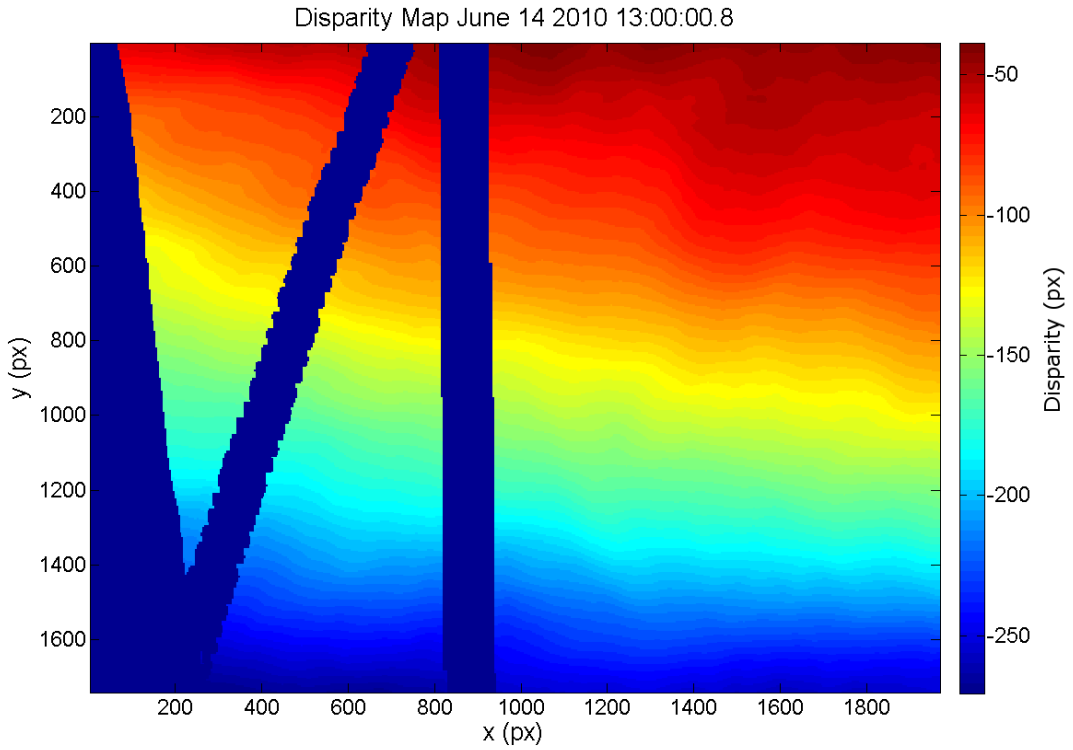

Figure 2.7: Example of a disparity map in pixels. Each point represents the distance between corresponding areas in the left and right rectified images. Areas where the cameras do not overlap, or which were obscured by the mooring line are excluded.

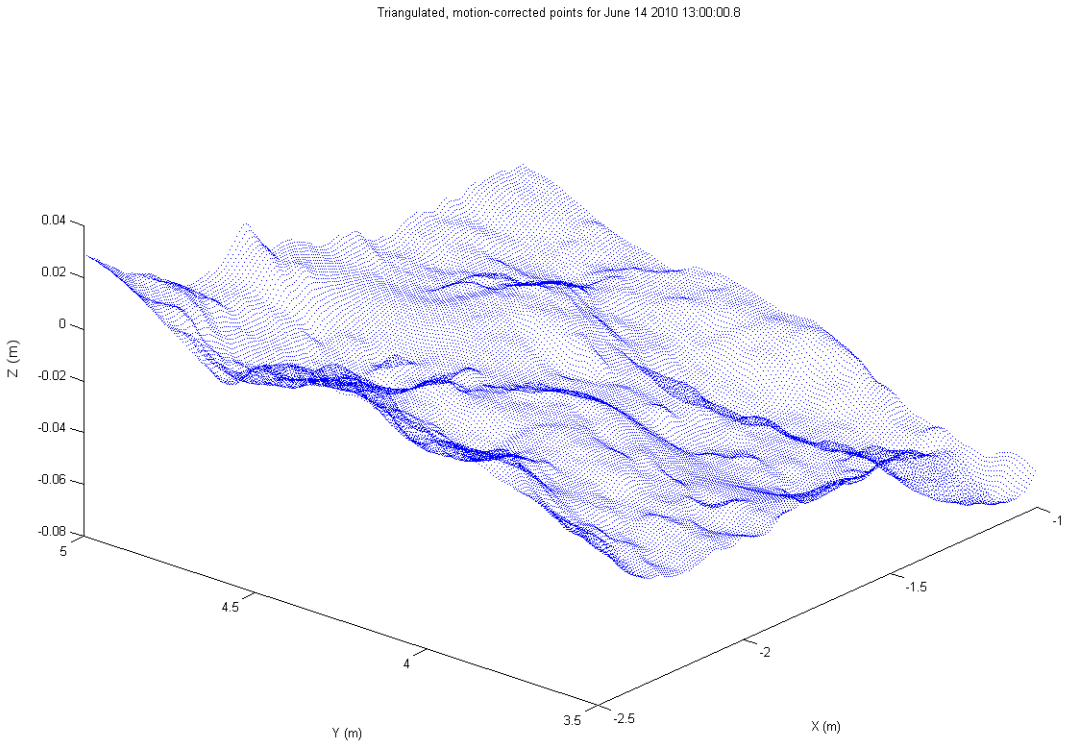

Figure 2.8: Example of a portion rotated point cloud (June 14 2010 13:00:00.8). Each XYZ triplet corresponds to one datapoint in the disparity map.

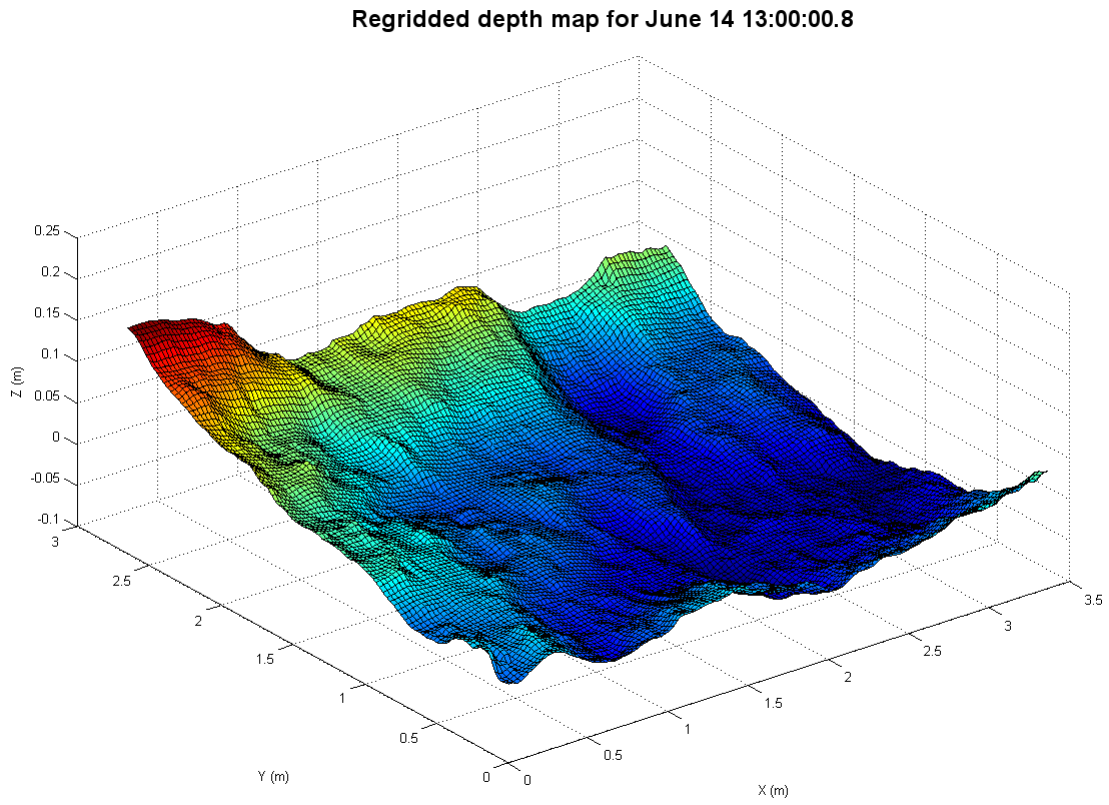

Figure 2.9: The final step is generating a depth map on a regular grid from the triangulated point cloud. This is the final depth map for June 14 13:00:00.8 with a horizontal resolution of $2.5cm$.

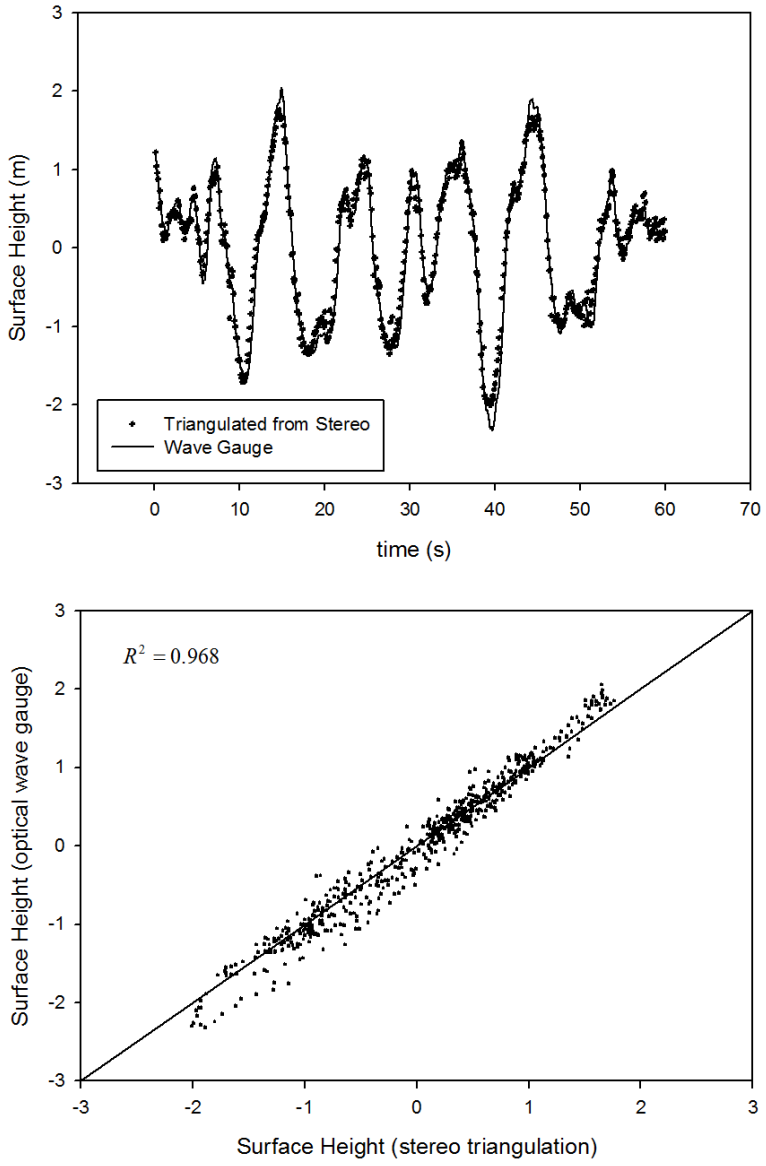

Figure 2.10: Range comparison between optical wave gauge and stereo system from June 14 2010 13:00. The mean wind speed was 13.13 m/s.

Chapter 3

WAVE STATISTICS

In this chapter the depth maps are analyzed to calculate relevant spatial and temporal statistics of the wave field.

3.1 Wave Spectra

Following *Phillips* (1977), the three dimensional spectrum, defined as the fourier transform of the covariance of the surface displacement, may be calculated:

$$Z(\overrightarrow{r},\tau) = \overline{\eta(\overrightarrow{\mathbf{x}},t)\eta(\overrightarrow{\mathbf{x}}+\overrightarrow{\mathbf{r}},t+\tau)} \tag{3.1}$$

$$\chi(\overrightarrow{\mathbf{k}},\omega) = (2\pi)^{-3}\int_{\tau}\int_{\overrightarrow{\mathbf{r}}} Z(\overrightarrow{\mathbf{r}},\tau)e^{-i(\overrightarrow{\mathbf{k}}\cdot\overrightarrow{\mathbf{r}}-\omega\tau)}\overrightarrow{\mathbf{dr}}d\tau \tag{3.2}$$

This allows for a characterization of the wave field in the frequency and wavenumber domains. The directional wavenumber spectrum, a measure of the orientation of the wave field as a function of wavenumber, is given as

$$\Phi(\overrightarrow{\mathbf{k}}) = 2\int_0^{\infty}\chi(\overrightarrow{\mathbf{k}},\omega)d\omega \tag{3.3}$$

The directional frequency spectrum, a measure of the orientation of the wave field as a function of frequency, is

$$\varphi(\omega,\theta) = 2\int_0^{\infty}\chi(\overrightarrow{\mathbf{k}},\omega)k\ d\overrightarrow{\mathbf{k}} \tag{3.4}$$

where $k = |\overrightarrow{\mathbf{k}}| = \sqrt{k_1^2 + k_2^2}$. The omnidirectional wavenumber spectrum, a measure of the sum-total surface height variance as a funcion of wavenumber k, is

$$\phi(k) = \int_{-\pi}^{\pi} \Phi(k, \theta) k d\theta \tag{3.5}$$

where $\Phi(k, \theta)$ is the directional wavenumber spectrum transformed from cartesian (k_1, k_2) to polar $(|\overrightarrow{\mathbf{k}}|, \theta)$ coordinates. The frequency spectrum, a measure of surface height variance as a function of frequency, is defined as

$$S(\omega) = \int_{-\pi}^{\pi} \varphi(\omega, \theta) d\theta \tag{3.6}$$

Frequency spectra, calculated in this instance from a time series of the mean surface height taken from a $10cm \times 10cm$ area at the center of each elevation map, is given in Figure 3.1 . A line with slope f^{-4}, the form predicted by *Phillips* (1985) is shown for reference.

If we assume a linear dispersion relationship $\omega^2 = gk$, we can say something about the relationship between the forms of the frequency and omnidirectional wavenumber spectra. These relationships may not hold in the field as the dispersion relationship is modified from the linear theory due to the currents generated by the long wave. Mainly, we can say

$$S(\omega) = \frac{2\omega^3}{g^2} \int_{-\pi}^{\pi} \Phi(k, \theta) d\theta \tag{3.7}$$

when $k = \omega^2/g$. This is the relationship between the frequency spectrum and the directional wavenumber spectrum. Practically this equation can be used to go back

and forth between frequency and wavenumber domains. This treatment leads to an omnidirectional spectrum with a predicted slope of $k^{-2.5}$ if a frequency spectrum $S(\omega)$ is of the form ω^{-4}.

The data generated using the methods outlined in chapter 2 have great potential to provide direct insight into the evolution of the wave spectrum at small scales ($5 < k < 50\ rad/m$). These data are unique in that they offer a dense, 4-dimensional (x, y, z, t) description of the surface waves for varying sea-states. As outlined in the introduction, it is extremely important to better understand the physical processes occurring at these scales. In the short term, knowledge of the small-scale wave field may be used to more accurately calibrate wave-sensing radar and satellite instruments. Also, in order to accurately model larger climate processes, it may be necessary to directly include the influence of these waves.

Figure 3.2 gives omnidirectional wavenumber spectra calculated from surface elevation maps for several ten minute periods during the HIRES experiment. They show $\phi(k)$ is of the form k^{-3} at these scales ($k = 1 - 50\,rad/m$). This form agrees with *Phillips* (1958) and *Kitaigorodskii* (1983), rather than the later form of *Phillips* (1985). A similar result was shown in *Banner* (1989). In a separate field experiment, *Romero and Melville* (2010) showed there may be a region close to the spectral peak where the form of the omnidirectional spectrum transitions from the form predicted in *Phillips* (1985) to the earlier result of *Phillips* (1958). The spectra from that experiment are plotted in Figure 3.2 (upper left) for reference. Although data at these scales are scarce, these results are consistent with those available. It also interesting to note that the relative energy levels of the calculated omnidirectional spectra from this experiment do not at first glance appear to be a function of mean wind speed.

Directional wavenumber spectra are presented in Figures 3.3 and 3.4. Figure 3.3, a collection of mean directional spectra, each calculated from ten minutes of elevation data, shows a mean wave field which appears to be largely spatially isotropic at these scales. The instantaneous directional spectra, examples of which are given in Figure 3.3, show a sometimes highly directionally organized spatial wave field. The constantly changing directionality which leads to an isotropic mean directional wavenumber spectrum in the wavenumber range studied here may be caused by variability in the wind direction, wave breaking, wave current interaction, air-flow separation, and/or wave-wave interactions. There is potential that in studying the evolution of the directional spectrum, a better understanding of these relationships may be achieved.

3.2 Phase-Averaged Quantities

A logical extension of this work is to investigate how waves of different scales interact. In order to see if the variance in the elevation maps caused by small waves was a function of the peak wave phase, a peak wave phase value was assigned to each of the 6000 elevation maps for each dataset. This was accomplished by taking the Hilbert transform of the mean surface height record. The elevation maps were then band-pass filtered for two distinct wavenumber bands ($k = 10,\ k = 15\, rad/m$). The mean variance of the band-pass filtered images was then calculated and recorded. The phase averaged results are given in Figures 3.5 and 3.6. A phase of 0 corresponds to the peak-wave crest, while phases of $\pm c\pi/2$ correspond to the front and back face of the peak-wave, respectively.

Several previous investigations have shown a propensity for small waves riding on large waves to group near the larger wave crests. Due to the orbital velocity of the longer wave, the small waves become shorter and steeper at the long-wave crests (*Longuet-Higgins and Stewart*, 1960). It is also possible that with such large waves (H_s up to 5 m), wave generating energy from the wind is a function of peak wave phase.

This is not meant to be a conclusive result, rather a promising start to a more thorough investigation. These limited data show enhanced wave-elevation variance due to small waves at the crests of the peak waves.

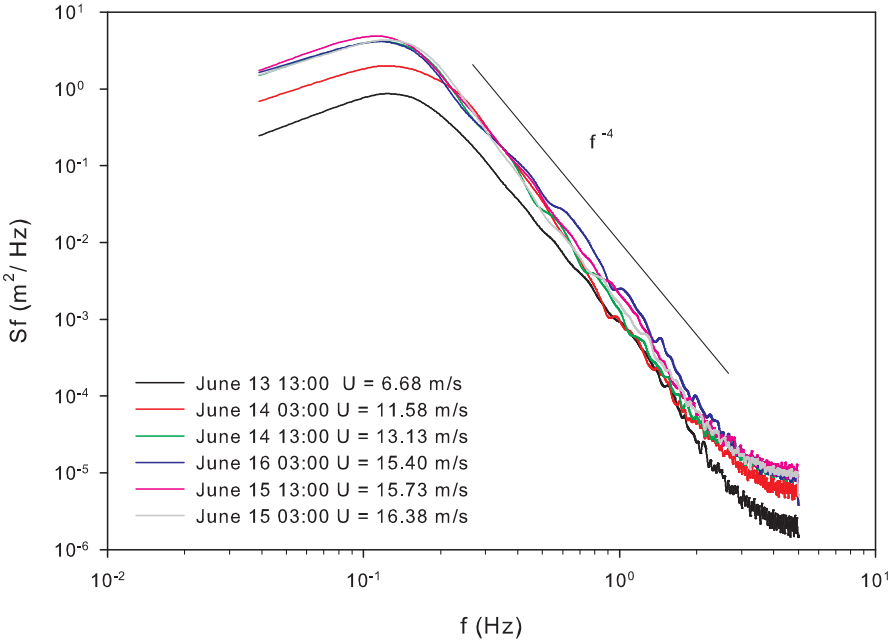

Figure 3.1: Frequency spectra for several experiment runs with wind speeds ranging from 6.68 to 16.38 m/s

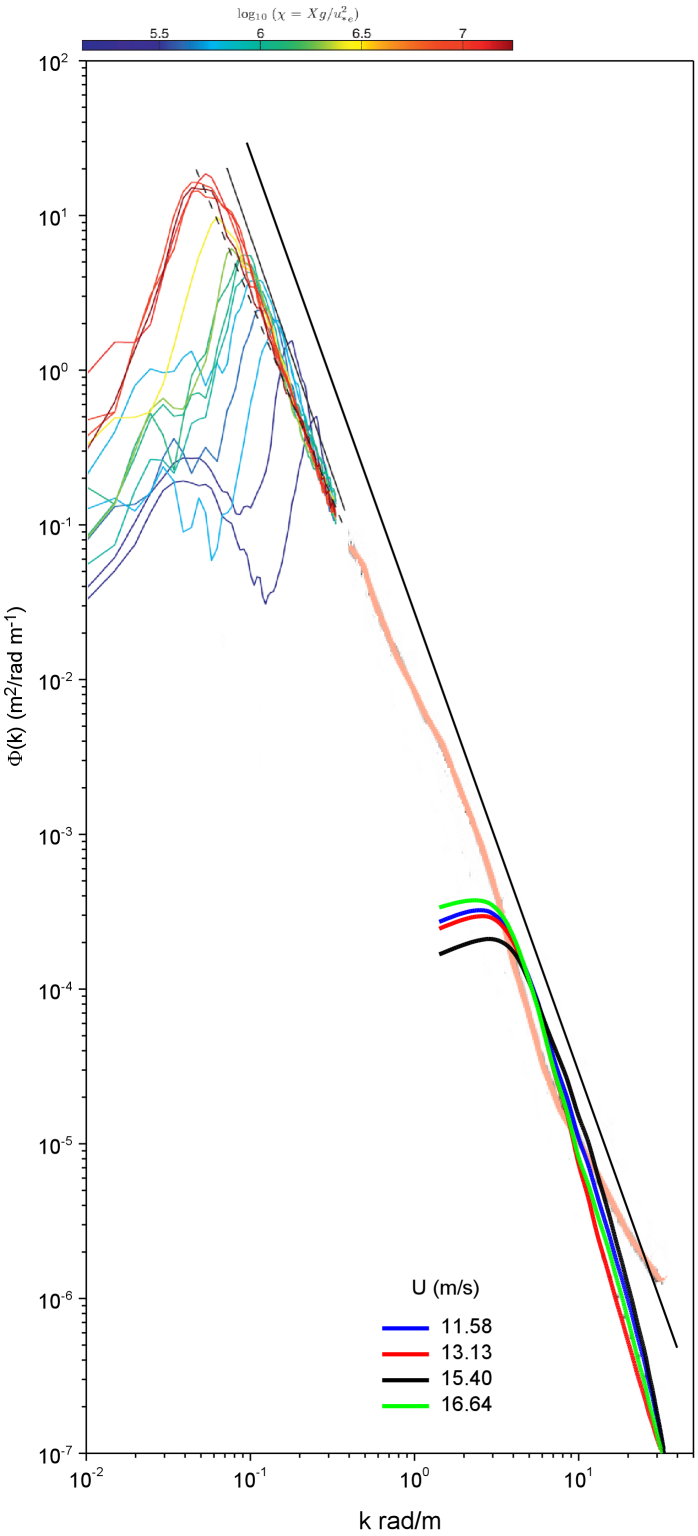

Figure 3.2: Omnidirectional spectra are plotted for several ten-minute datasets (lower right). Omnidirectional spectra from *Romero and Melville* (2010) (upper left) and from *Benetazzo et al.* (2012) (beige) are plotted for reference. The solid line shows a k^{-3} slope, while the dashed line shows $k^{-2.5}$.

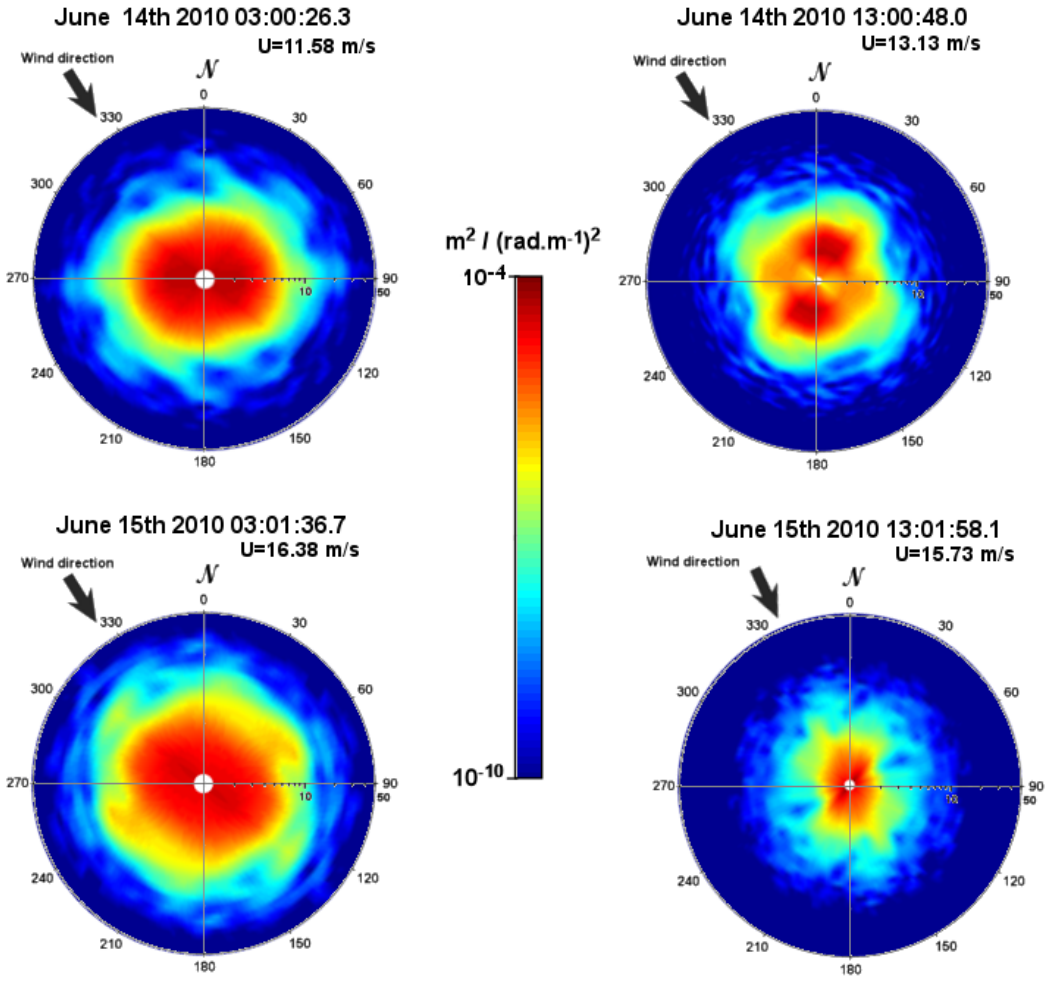

Figure 3.3: Instantaneous directional spectra show wave fields with unique directional characteristics.

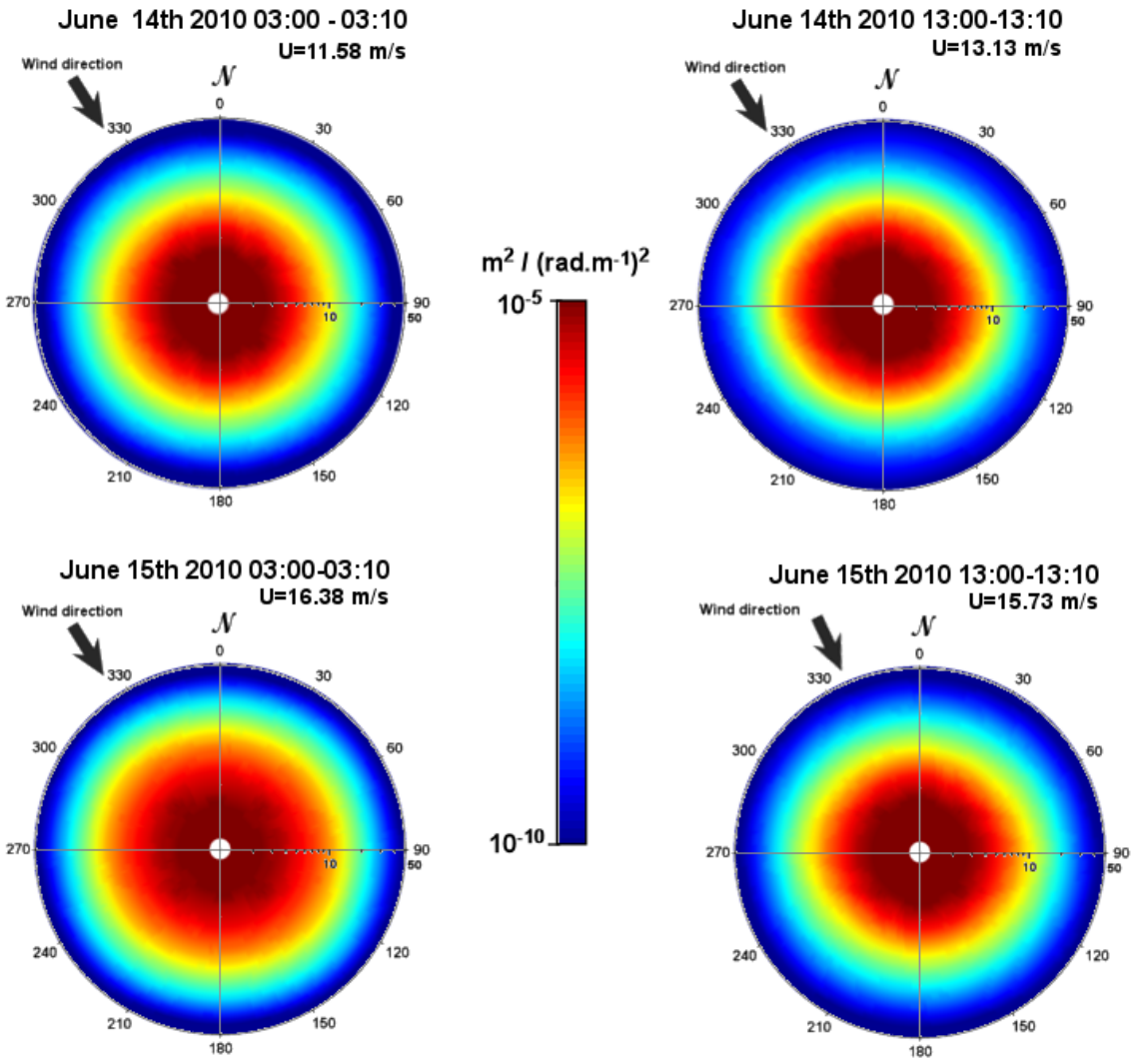

Figure 3.4: 10-minute mean directional wavenumber spectrums from 4 of the datasets analyzed. All mean directional spectra show a practically isotropic form for the wavenumber range studied here.

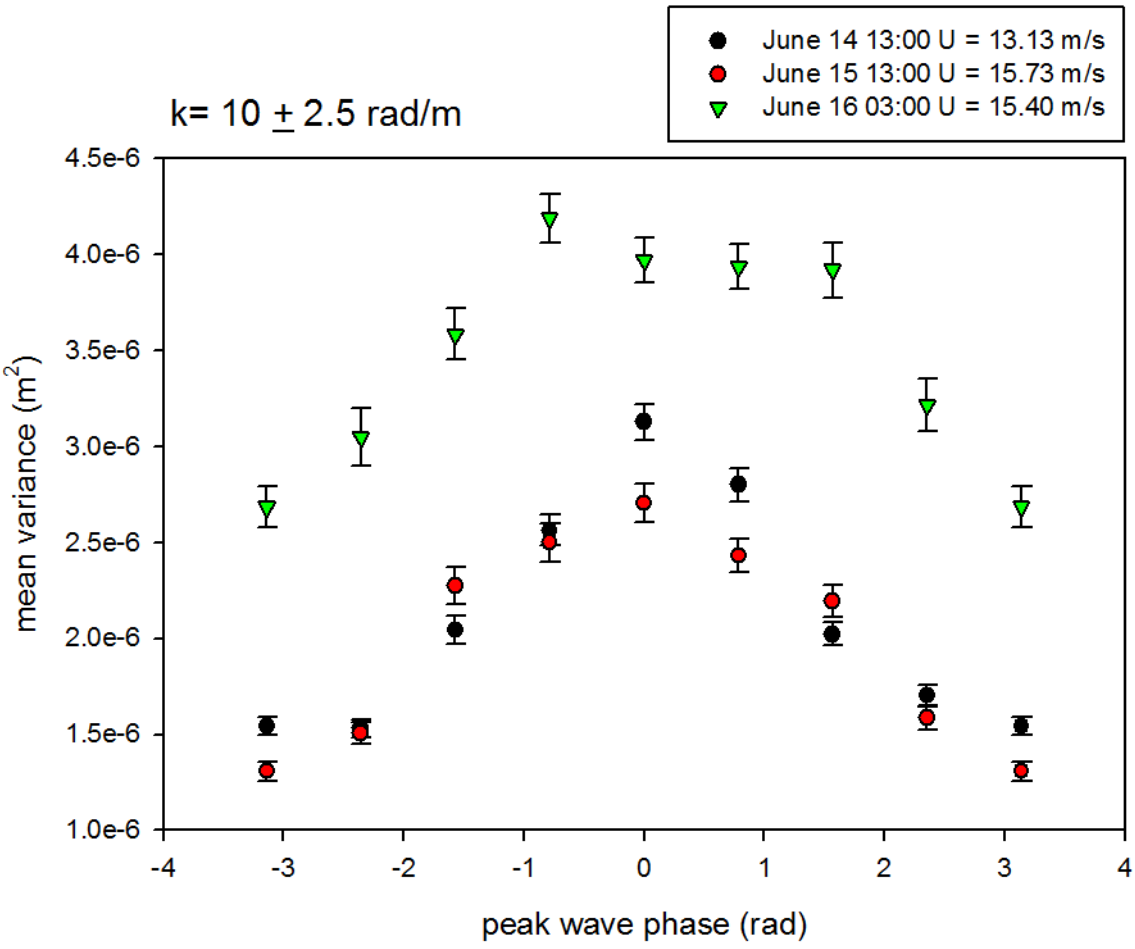

Figure 3.5: Phase averaged mean variance for $k = 10\,rad/m$. Error bars represent 90 % confidence intervals.

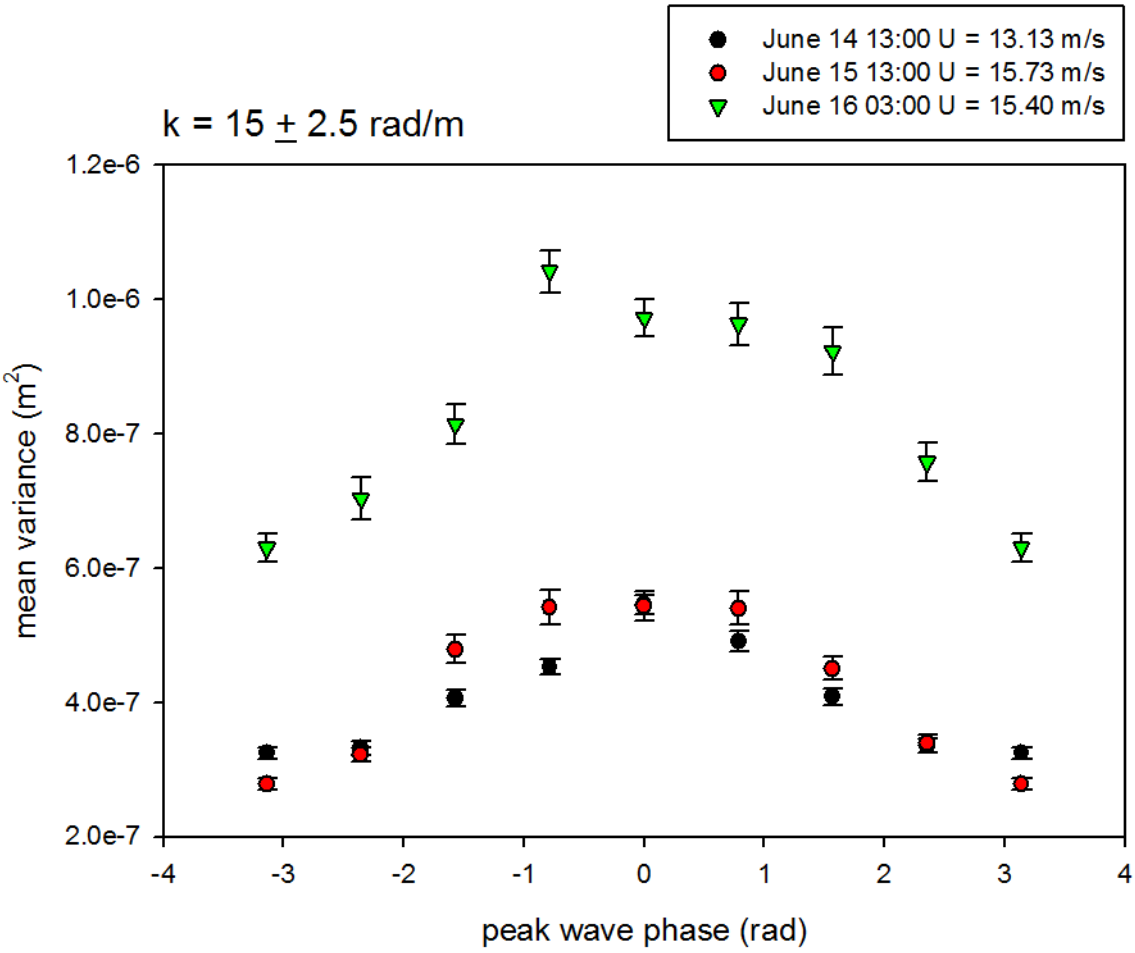

Figure 3.6: Phase averaged mean variance for $k = 15\,rad/m$. Error bars represent 90 % confidence intervals.

Chapter 4

CONCLUSION

In this investigation, a novel method was developed to convert stereo video data to 3-dimensional elevation maps. The hybrid variational, cross-correlation algorithm developed here was used to reconstruct the wave field for several ten minute periods during June 2010 off the coast of Santa Rosa, CA. Field data at this scale and for these conditions are extremely scarce, and should provide an excellent resource for future investigations. In particular, studying the evolution of the directional wavenumber spectrum, as well as investigating the wavenumber-frequency spectrum, may offer additional value.

The spectral analysis of these data show good agreement with other investigations, and provide new insight into the physics of surface gravity waves at small scales. An omnidirectional wavenumber spectrum of the form k^{-3} was observed, agreeing with the results of *Phillips* (1958); *Kitaigorodskii* (1983); *Banner* (1989); *Romero and Melville* (2010), and others. The mean directional wavenumber spectrum was found to be largely isotropic.

Lastly, small-scale surface-height variance was calculated as a function of the peak wave phase. The result seemed to validate the idea that smaller-waves are concentrated at the crests of larger waves, although a more thorough analysis is needed to quantify these interactions.

It cannot be emphasized enough that if we are to more completely understand large climatological processes, we need to better understand the physics occurring at the air-sea interface. This relatively small region is largely responsible for regulating the flux of heat, momentum, moisture, and gasses between the two fluids. This investigation offers a small but nonetheless valuable contribution towards that aim.

Bibliography

Banner, M. L. (1989), Wavenumber spectra of short gravity waves, *Journal of Fluid Mechanics*, *198*, 321–344.

Banner, M. L., and W. K. Melville (1976), On the separation of air flow over water waves, *Journal of Fluid Mechanics*, *77*(4), 825–842.

Benetazzo, A., F. Fedele, G. Gallego, P.-C. Shih, and A. Yezzi (2012), Offshore stereo measurements of gravity waves, *Coastal Engineering*, *64*, 127–138.

Bouguet, J. (2011), Camera calibration toolbox, *http://www.vision.caltech.edu/bouguetj/calib_doc/*.

Cochran, S. D., and G. Medioni (1992), 3-d surface description from binocular stereo, *IEEE Transactions on Pattern Analysis and Machine Intelligence*, *14*(10), 981–994.

Faugeras, O., and R. Keriven (2002), Variational principles, surface evolution, pde's, level set methods and the stereo problem, in *Biomedical Imaging, 2002. 5th IEEE EMBS International Summer School on Biomedical Imaging*, pp. 83–pp, IEEE.

Fusiello, A., and L. Irsara (2008), Quasi-euclidean uncalibrated epipolar rectification, in *Pattern Recognition, 2008. ICPR 2008. 19th International Conference on*, pp. 1 –4, doi:10.1109/ICPR.2008.4761561.

Gallego, A. B., A. Yezzi, and F. Fedele (2008), Wave statistics and spectra vis a variotnal wave acquisition system, International Conference on Pattern Recognition (ICPR), Tampa, FL.

Jähne, B., and S. Waas (1994), Imaging of short ocean wind waves: a critical theoretical review, *J. Opt. Soc. Am. A*, *11*, 198–227.

Kitaigorodskii, S. (1983), On the theory of the equilibrium range in the spectrum of wind-generated gravity waves, *Journal of Physical Oceanography*, *13*(5), 816–827.

Le Quéré, C., et al. (2007), Saturation of the southern ocean co_2 sink due to recent climate change, *science*, *316*(5832), 1735–1738.

Liu, W. T. (2002), Progress in scatterometer application, *Journal of Oceanography*, *58*(1), 121–136.

Longuet-Higgins, M. S., and R. W. Stewart (1960), Changes in the form of short gravity waves on long waves and tidal currents, *Journal of Fluid Mechanics*, *8*, 565–583, doi: 10.1017/S0022112060000803.

Melville, W. K. (1996), The role of surface-wave breaking in air-sea interaction, *Annual review of fluid mechanics*, *28*(1), 279–321.

Naderi, F. M., M. H. Freilich, and D. G. Long (1991), Spaceborne radar measurement of wind velocity over the ocean-an overview of the nscat scatterometer system, *Proceedings of the IEEE*, *79*(6), 850–866.

Phillips, O. M. (1958), The equilibrium range in the spectrum of wind-generated waves, *J. Fluid Mech*, *4*(4), 426–434.

Phillips, O. M. (1977), *The Dynamics of the Upper Ocean*, 102-106 pp., Cambridge University Press.

Phillips, O. M. (1985), Spectral and statistical properties of the equilibrium range in wind-generated gravity waves, *Journal of Fluid Mechanics*, *156*, 505–531.

Romero, L., and W. K. Melville (2010), Airborne Observations of Fetch-Limited Waves in the Gulf of Tehuantepec, *Journal of Physical Oceanography*, *40*(3), 441–465, doi: 10.1175/2009JPO4127.1.

Scharstein, D., and R. Szeliski (2002), A taxonomy and evaluation of dense two-frame stereo correspondence algorithms, *International journal of computer vision*, *47*(1), 7–42.

Shemdin, O., H. Tran, and S. Wu (1988), Directional measurement of short ocean waves with stereophotography, *Journal of Geophysical Research*, *93*(C11), 13,891–13.

Wanek, J. M., and C. H. Wu (2006), Automated trinocular stereo imaging system for three-dimensional surface wave measurements, *Ocean Engineering*, *33*(56), 723 – 747, doi:10.1016/j.oceaneng.2005.05.006.